

pubs.acs.org/NanoLett Letter

# Relativistic Light Sails Need to Billow

Matthew F. Campbell, John Brewer, Deep Jariwala, Aaswath P. Raman, and Igor Bargatin\*



Cite This: Nano Lett. 2022, 22, 90-96



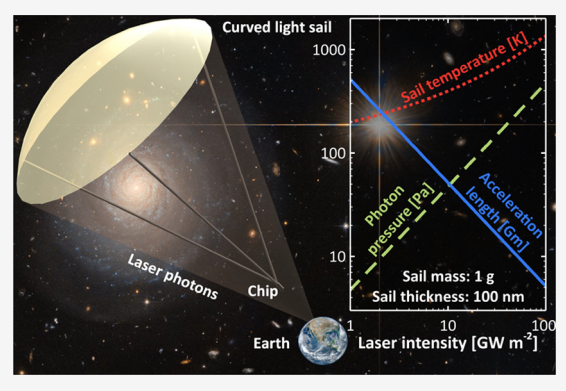
**ACCESS** 

Metrics & More

Article Recommendations

SI Supporting Information

ABSTRACT: We argue that light sails with nanometer-scale thicknesses that are rapidly accelerated to relativistic velocities by lasers must be significantly curved in order to reduce their intrafilm mechanical stresses and avoid tears. Using an integrated opto-thermo-mechanical model, we show that the diameter and radius of curvature of a circular light sail should be comparable in magnitude, both on the order of a few meters, in optimal designs for gram-scale payloads. Moreover, we demonstrate that, when sufficient laser power is available, a sail's acceleration length decreases as its curvature increases. Our findings provide critical guidance for emerging light sail design programs, which herald a new era of interstellar space exploration to destinations such as the Oort cloud, the Alpha Centauri system, and beyond.



KEYWORDS: Laser propulsion, Membrane stress, Molybdenum disulfide, Photon pressure, Relativistic light sail

ur knowledge about life on other planets is currently limited by the energy density of rocket fuels, <sup>1,2</sup> by the resolution of Earth-based and orbiting telescopes, <sup>3</sup> and by the scarcity of interstellar objects observed while passing through our solar system. <sup>4</sup> Light sails with nanometer-scale thicknesses towing gram-scale microchip payloads <sup>5</sup> that are accelerated to relativistic velocities by high-power lasers have the potential to significantly increase humankind's understanding of the cosmos. <sup>6-9</sup> In particular, recent discoveries of exoplanets in the Alpha Centauri system <sup>3,10-12</sup> have prompted the Starshot Breakthrough Initiative <sup>7,8</sup> to set Proxima Centauri, a star located about 4.2 ly away from Earth, as a target destination for light sail development. Previous studies have examined light sails in terms of their optical properties, <sup>13-20</sup> laser-beam-riding stability, <sup>14,21-29</sup> and interaction with the interstellar medium <sup>30-32</sup> but have largely overlooked their ability to sustain the intense photon pressures required for their acceleration.

Light sails' ability to withstand their intrafilm stress and strain, caused by the laser-induced photon pressure, dictates their survivability and ultimately may determine the success of their interstellar missions. Several authors have examined the mechanics of *solar* sails, which are sunlight-driven analogues to laser-propelled light sails. However, solar sails generally experience much lower photon pressures and accelerations in comparison to coherent-photon-driven light sails, such that the primary concern of photon-induced deformation in solar sails is trajectory alteration rather than sail breakage. To our knowledge, only a single paper has considered structural mechanics issues for a laser-powered light sail undergoing high acceleration: in particular, focusing on the wrinkling instabilities of a square-planar sail and providing bending stiffness design guidelines. We are unaware of any work

examining the photon-pressure-induced stresses and strains in curved sails, which also benefit from their passive laser-beam-riding stability. Here, we consider a generic spherically curved circular sail with gram-scale mass, square-meter-scale area, and nanometer-scale thickness that tows a gram-scale-mass chip-satellite payload (Figure 1) and analyze its photon-flux-induced stress and strain in terms of key design dimensions and material property limitations. We will show that light sails must be significantly curved in order to prevent tears. This conclusion mirrors the behavior of parachutes and

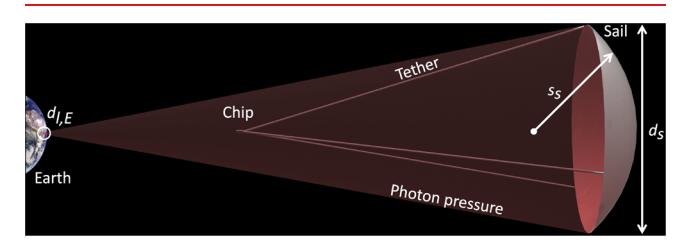


**Figure 1.** Concept diagram of a curved circular light sail towing a chip-satellite using three tethers (not to scale). The sail has a perpendicular to beam diameter  $d_s$  and spherical radius of curvature  $s_s$  and is accelerated by an array of Earth-bound lasers whose diameter is  $d_{\rm LE}$ . Earth image obtained from NASA.<sup>39</sup>

Received: August 24, 2021
Revised: December 6, 2021
Published: December 23, 2021





wind sails of sailboats, which can also minimize pressure-induced stresses by billowing, 36,37 as well as the typical (spherical or cylindrical) shapes of lightweight pressure vessels. 38

We begin by introducing three high-level light sail design tradeoffs that will guide our numerical analysis. Consider the light sail pictured in Figure 1, which has diameter  $d_s$ , spherical radius of curvature  $s_{st}$  and sail film thickness  $t_{f}$ . The first tradeoff involves the sail curvature, which, for a given sail diameter, increases as  $s_s$  is reduced (the sail becomes more curved). If the sail is too curved (for  $s_s < \frac{d_s}{\sqrt{2}}$ ), laser light incident on its perimeter will be reflected toward the perimeter on its opposite side, resulting in a multireflection process that is associated with additional absorption and heating. If the sail is too flat (large  $s_s$ ), the sail may be unstable on the laser beam<sup>21</sup> and also may experience excessive bending or tensile stresses. The second tradeoff involves the sail film thickness  $t_f$ . Sails that are very thick tend to exhibit high absorption of incident laser light and thus overheat, whereas sails that are vanishingly thin exhibit low reflectivities and therefore accelerate slowly. The third tradeoff concerns the diameter  $d_s$ . For a fixed incident laser power that is perfectly focused on the sail area, sails with smaller diameters experience greater photon intensities and are subject to overheating. In contrast, since the minimum sail film thickness has a lower bound of a few atoms at best, sails with large diameters must become more massive and hence will accelerate more slowly. These sail design tradeoffs are also interrelated: For a given sail mass  $m_s$ ,  $t_f$  scales inversely with the film density  $\rho_f$  and sail surface area  $A_s$ , which for spherically curved sails depends on both  $d_s$  and  $s_s$ :  $t_f = \frac{m_s}{\rho_f A_s(d_s, s_s)}$  (see Section S2 in the Supporting Information).

To understand the intricate interactions of these design parameters, we developed a multiphysics sail model that uses a single effective hybrid material based on the properties for molybdenum disulfide (MoS<sub>2</sub>) and alumina (Al<sub>2</sub>O<sub>3</sub>), which have desirable optical, thermal, mechanical, and manufacturability attributes for light sails.  $^{9,40-48}$  As discussed in Section S9 in the Supporting Information, the single-layer hybrid effective-material model adequately describes the behavior of multilayer composite sails made from MoS<sub>2</sub> and Al<sub>2</sub>O<sub>3</sub> while greatly simplifying the optical, thermal, and mechanical analyses. Despite the simplicity of this model, the fundamental insights it uncovers should translate to more complex sail designs and future alternative materials as well.  $^{49,50}$ 

Using this model, we first examine the sail's acceleration length, photon pressure, and equilibrium temperature and determine how these scale in relation to fundamental design properties. The acceleration length L, or the distance the sail travels while being illuminated by laser-generated photons, is a key figure of merit for light sail design; it scales as  $L \sim \frac{m_{\rm tot} c \nu_1^2}{2\Phi_1 \varrho_a}$ , where  $m_{\rm tot}$  is the total mass of the sail, chip, and tethers, c is the speed of light,  $v_{\rm f}$  is the final sail velocity,  $\Phi_{\rm l}$  is the laser output power, and  $\varrho_{\rm a}$  is the sail's average reflectivity near the laser wavelength. As the sail accelerates over this distance, it will feel an effective photon pressure P, caused by the impinging and reflecting laser light, which scales as  $P \sim \frac{8\Phi_1 \varrho_1}{\pi c d_s^2}$ , where  $\varrho_{\perp}$  is the normal-incidence reflectivity at the center of the sail (for the relationship between  $\varrho_{\perp}$  and  $\varrho_{\rm av}$  see Section S7 in the Supporting Information). In addition, the sail will absorb a

small fraction of the incoming laser power and achieve an equilibrium temperature T, at which it radiatively emits an equal amount of power. This temperature scales as  $T^4 \sim \frac{2\alpha_{\rm L}\Phi_{\rm L}}{\pi\varepsilon_{\rm c}\sigma d_{\rm s}^2}$ , where  $\alpha_{\perp}$  and  $\varepsilon_{\rm e}$  are the perpendicular-to-sail absorptivity near the laser wavelength and the effective hemispherical emissivity of the sail, respectively, and  $\sigma$  is the Stefan–Boltzmann constant. We note that, in general, the emissivity and absorptivity are themselves functions of temperature, but in this simplified analysis we have fixed them at their room-temperature values.

Before delving into the mechanical stresses of a curved sail, we first consider just the photon pressure and the equilibrium temperature in the simple case of an infinitely strong and flat (noncurved) light sail with perpendicular-to-the-laser-beam area  $A_{\perp}$  accelerated under constant laser output power  $\Phi_{\rm l}$ . In Figure 2 we show the scaling of these parameters, as well as the

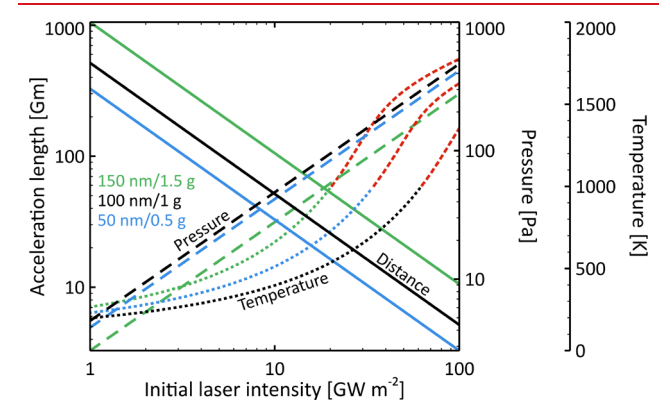


Figure 2. Acceleration length L (solid lines), peak center pressure  $P_{\rm max}$  (dashed lines), and peak center temperature  $T_{\rm max}$  (dotted lines) of a flat (noncurved)  $A_{\perp} = 2 \text{ m}^2$  area light sail composed of the effective  $MoS_2/Al_2O_3$  hybrid material as a function of the initial laser light intensity on the sail  $I_{s,0} = \frac{\Phi_1}{A_L}$  when the sail mass is  $m_s = \frac{1}{2} m_{\text{tot}}$ , which is the optimal ratio for flat sails. 13,51 Here and elsewhere we use a laser output wavelength of  $\lambda_{\rm l}$  = 1.2  $\mu$ m and assume a final sailcraft velocity of  $v_f = \frac{c}{5}$ , which is appropriate for an approximately 21 year mission to Proxima Centauri, a star located about 4.2 ly away from Earth.<sup>7,8</sup> Color code: green (sail film thickness  $t_f = 150$  nm, sail mass  $m_s = 1.5 \text{ g}$ ; black ( $t_f = 100 \text{ nm}$ ,  $m_s = 1 \text{ g}$ ); blue ( $t_f = 50 \text{ nm}$ ,  $m_s = 0.5 \text{ m}$ g). The red dashed lines indicate temperatures above the ultrahigh vacuum sublimation point of MoS<sub>2</sub> ( $T_{\text{sub}} \approx 1000 \text{ K}$ ). <sup>43,44</sup> Due to constructive interference, thicknesses near 100 nm offer the highest reflectivity (i.e., the highest photon pressure) along with relatively low absorption, resulting in short acceleration distances and low temperatures. By comparison, relative to the 100 nm sail, the 50 nm sail has 50% lower  $m_s$  (thus allowing it to achieve shorter acceleration distances), 19% lower  $\overline{Q}_{a}$  (thereby causing slightly lower photon pressure), 15% higher  $\overline{\alpha_1}$ , and 42% lower  $\varepsilon_e$  (thus causing it to have a higher temperature). (In these quantities, the overbar symbol denotes spectral averaging over the Doppler-shifted laser wavelength range.)

resulting acceleration distance to a final sailcraft velocity of  $v_{\rm f} = \frac{c}{5}$ , as a function of the initial (near Earth) laser light intensity on the sail  $I_{\rm s,0} = \frac{\Phi_{\rm l}}{A_{\rm l}}$  and the sail mass  $m_{\rm s}$ . Since P and T change throughout the acceleration phase (see Sections S3 and S4 in the Supporting Information), we have selected only the maximum values within each trajectory,  $P_{\rm max}$  and  $T_{\rm max}$  respectively, for this graphic. Importantly, cases with the

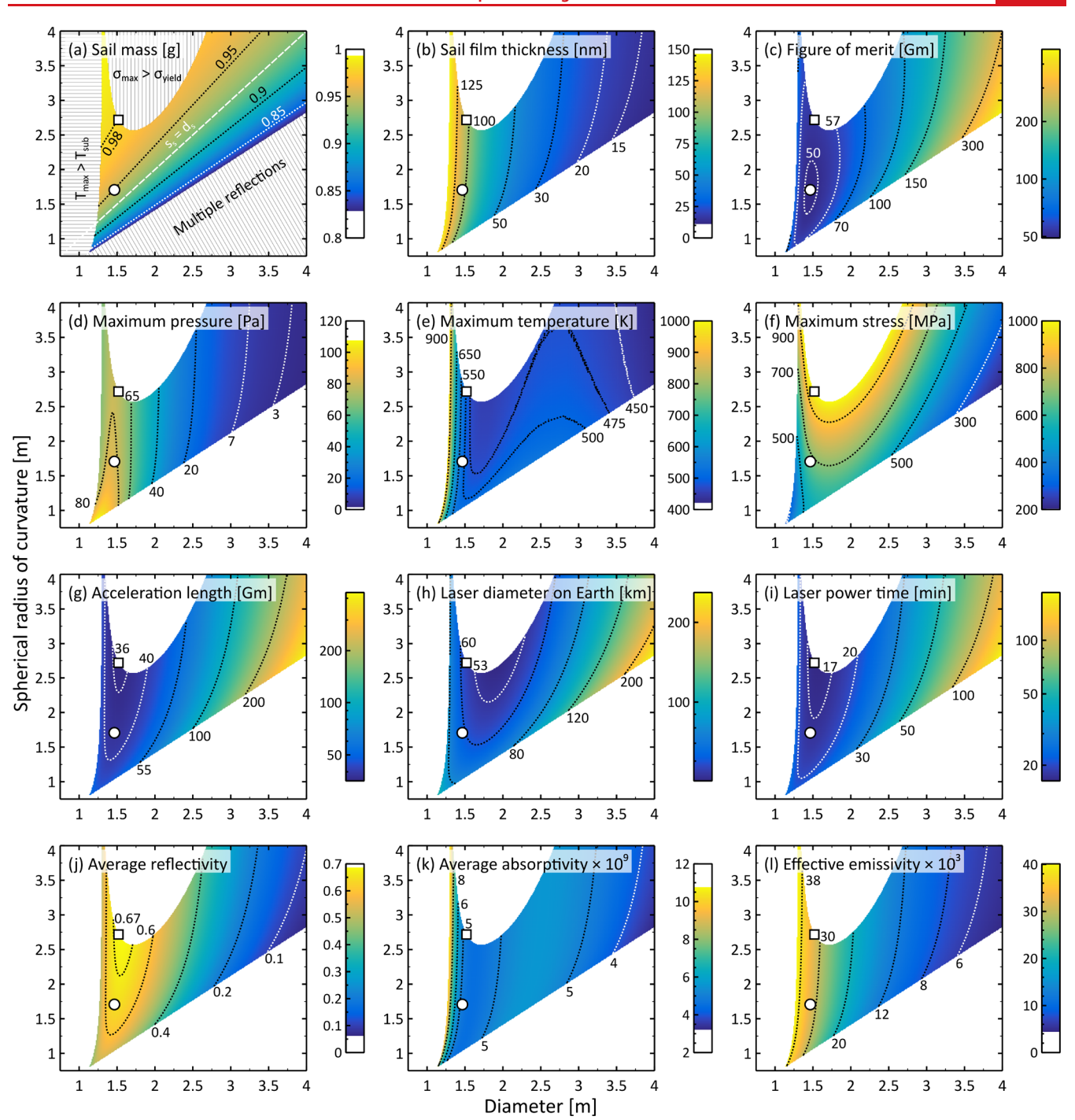


Figure 3. (a) Sail mass  $m_{s_r}$  (b) film thickness  $t_p$  (c) figure of merit  $\mathcal{F}$  (eq 1), (d) maximum pressure  $P_{\text{max}}$  (e) maximum temperature  $T_{\text{max}}$  (f) maximum stress  $\sigma_{s,\text{max}}$  (g) acceleration length L, (h) laser diameter on Earth  $d_{\text{l,E}}$  (i) laser power time  $t_{\text{l}}$  (j) average reflectivity  $\overline{Q_a}$ , (k) average absorptivity  $\overline{Q_a}$ , and (l) effective emissivity  $\varepsilon_{\text{e}}$  for a light sail composed of the effective MoS<sub>2</sub>/Al<sub>2</sub>O<sub>3</sub> hybrid material with  $m_{\text{tot}} = 2$  g,  $\Phi_{\text{l}} = 30$  GW,  $\lambda_{\text{l}} = 1.2$   $\mu$ m, and  $v_{\text{f}} = \frac{c}{5}$  (in these quantities the overbar symbol denotes spectral averaging). The dashed line in (a) denotes circular diameter and spherical radius of curvature equivalence:  $d_s = s_s$ . The squares denote the  $d_s - s_s$  design exhibiting the minimum value of L, and the circles denote that with the minimum value of  $\mathcal{F}$ . The  $\overline{d_1}$  values of (k), though small, reflect the low extinction coefficients  $\kappa$  of MoS<sub>2</sub> and Al<sub>2</sub>O<sub>3</sub> near the laser wavelength  $d_s = 1.25$  m and  $d_s = 1.25$  m, while technically viable alternatives, are not robust design choices because small manufacturing imperfections could cause them to overheat or tear.

lowest acceleration lengths L suffer from excessively high pressures and temperatures, implying that mechanical and thermal factors place strong constraints on light sail designs and must be balanced against metrics such as the acceleration length.

Next, we consider the stress within the sail film that is caused by the photon pressure, for the case of a spherically curved round sail that is illuminated by an unpolarized laser beam with a uniform ("top hat") intensity profile. Importantly, the tensile stress  $\sigma$  experienced by the sail depends on its

curvature. In a flat (noncurved) sail, the light pressure is resisted by the sail's bending stiffness, resulting in a maximum tensile stress of  $\sigma_{\rm s,flat} \sim \frac{9Pd_{\rm s}^2}{32t_{\rm l}^2}$ . In contrast, that of spherically curved sails is resisted by tensile membrane stretching and scales as  $\sigma_{\rm s,curved} \sim \frac{Ps_{\rm s}}{2t_{\rm f}}$ . Using the minimum curvature of  $s_{\rm s} = \frac{d_{\rm s}}{\sqrt{2}}$  in order to minimize  $\sigma_{\rm s,curved}$ , the ratio of the stress in flat sails to that in curved sails can be estimated as  $\frac{\sigma_{\rm s,flat}}{\sigma_{\rm s,curved}} \sim \frac{d_{\rm s}}{t_{\rm f}} \gg 1$  because  $t_{\rm f}(\sim 100~{\rm nm}) \ll d_{\rm s}(\sim 1~{\rm m})$ , which means that curved sails experience much lower stresses than flat sails. Consequently, curved sails can sustain higher photon pressures  $P_{\rm s}$  allowing them to achieve lower acceleration lengths L relative to flat sails.

We now explore the effect of a sail's diameter  $d_s$  and radius of curvature  $s_s$  on its performance in order to provide general guidelines for light sail design. To aid this discussion, we have plotted 12 relevant quantities, including  $m_s$ ,  $t_t$ ,  $P_{max}$ ,  $T_{max}$ ,  $\sigma_{s,max}$  $L, \overline{Q}, \overline{\alpha}_{\perp}, \varepsilon_{e}$ , and three others that we will introduce below, as a function of  $d_s$  and  $s_s$  in Figure 3 for a  $m_{tot} = 2$  g sailcraft accelerated by a constant laser output power of  $\Phi_l$  = 30 GW (here the overbar symbol denotes spectral averaging over the Doppler-shifted laser wavelength range). In these panels, as labeled in Figure 3a, we have removed designs for which the curvature would result in multiple reflections and cause excessive heating in the center of the sail  $\left(s_{s} < \frac{d_{s}}{\sqrt{2}}\right)$ , designs hot enough to sublimate the material  $(T_{\rm max} > T_{\rm sub} \approx 1000 \, {\rm K}^{43,44})$ , and designs that would tear  $(\sigma_{\rm s,max} > \sigma_{\rm yield} \approx 1 \, {\rm K}^{43,46})$  $GPa^{45,46}$ ). Importantly, at low diameters  $d_s$ , few persisting light sail designs exhibit large radii of curvature s<sub>s</sub>, which underscores the imperative that light sails should be curved (higher s<sub>s</sub> values imply flatter structures). Put another way, light sails must be specifically designed to bow or billow in order to reduce the peak stresses they experience. 36,37,52

Further examination of Figure 3 reveals that most of the persisting designs feature similar diameter and radius of curvature values. This is highlighted by the white dashed line in Figure 3a, for which  $d_s = s_s$ , demonstrating a general principle that the diameter and radius of curvature of light sails must increase together. This fact can be explained by the scaling relationships introduced earlier, as well as by Figure 3d,f. Sails that have larger diameters experience lower pressures, and sails that have lower radii of curvature (sails that are more curved) experience lower tensile stress; such sails are therefore less likely to tear.

Figure 3a,b show the sail mass  $m_s$  and film thickness  $t_f$  values used in these calculations, respectively. In flat circular sails, the optimum sail mass is half the total sailcraft mass;  $^{7,13,51}$  however, the optimal mass of spherically curved round sails depends on  $d_s$  and  $s_s$ , and specifically,  $m_s$  decreases with increasing sail curvature (decreasing  $s_s$ ; see Figure 3a and Section S2 in the Supporting Information). This implies that sailcraft with billowing sails can allocate a greater fraction of the total mass budget to the chip and tethers in comparison to sailcraft with idealized flat sails. In addition, note from Figure 3b that, due to the  $m_{tot} = 2$  g constraint, the sail can be only tens of nanometers thick, emphasizing the importance of curvature to relieve stress.

The calculated acceleration length L values are provided in Figure 3g, and the  $d_s$ – $s_s$  design corresponding to the minimum L is indicated with the white square. A comparison with Figure

3f, however, shows that this point corresponds to  $\sigma_{s,max} = \sigma_{yield}$ , which has no failure margin. To identify designs with a higher probability of survival, we introduce a figure of merit  $\mathcal{F}$ 

$$\mathcal{F} = L \sqrt{1 + \left(\frac{\sigma_{\text{s,max}}}{\sigma_{\text{yield}}}\right)^2 + \left(\frac{T_{\text{max}}}{T_{\text{sub}}}\right)^2}$$
(1)

that accounts for the mechanical and thermal limitations of the sail. This definition includes both stress and thermal failure modes. If other failure methods, such as effects from interstellar dust,  $^{30-32}$  layer delamination in composite sails, or phase changes of the sail material, happen earlier, the figure of merit's definition can be adjusted accordingly. Values of  $\mathcal F$  are provided in Figure 3c, and the design corresponding to the minimum  $\mathcal F$  is shown with the white circle. This sail features a similar  $d_s$  but a lower  $s_s$  in comparison to the minimum L design, reducing the maximum tensile stress and strain by 34% while increasing the maximum temperature and acceleration length by only 4% and 6%, respectively. This simple figure of merit underscores the importance of including both mechanical and thermal factors in optimizing light sail designs.

The reason that the acceleration length L is often used as a figure of merit for light sail design is that it determines the diffraction-limited diameter of the phased laser array on Earth  $d_{\rm l,E} \sim 2\lambda_{\rm l} \frac{L}{d_{\rm s}}$  and the time duration for which the array must produce light  $t_{\rm l} \sim \frac{L}{v_{\rm l}}$ , which are important engineering design criteria for the photon engine (here  $\lambda_{\rm l}=1.2~\mu{\rm m}$  is the laser output wavelength).  $^{8,13,51,53-55}$  These quantities are provided in Figure 3h,i. Notice that the L and  $t_{\rm l}$  minima occur at similar  $d_{\rm s}$  values, whereas the minimum  $d_{\rm l,E}$  occurs at slightly larger  $d_{\rm s}$ , reflecting the laser array diameter's inverse sail diameter scaling. The surviving designs for both minima exhibit significant curvature.

Finally, we examine the effect of the sail diameter and radius of curvature on the optical properties of the sail and the corresponding implications for the light sail's performance. To begin, we stress that the optical properties of the sail film vary greatly with its thickness and can also depend on its photonically engineered structure. The film thickness in our calculations depends on the sail's diameter and spherical radius of curvature, since in Figure 3 we hold the total sailcraft mass  $m_{\text{tot}}$  constant (see Figure 3b and Section S2 in the Supporting Information). The  $d_s$  dependence is the cause of the horizontal variations in optical property values observable in Figure 3j-l, which show that  $\overline{Q}_a$ ,  $\overline{\alpha}_L$ , and  $\varepsilon_e$  generally increase with increasing  $t_f$  (i.e., decreasing  $d_s$ ). However, Figure 3j,k reveal that local reflectivity maxima and absorptivity minima exist (respectively), which are related to interference effects due to phases acquired by the electromagnetic wave as it travels in the film. 56 The film thickness corresponding to such optimal reflection scales inversely with the real component of the material's refractive index,  $t_{\rm f} \sim \frac{\lambda_1}{4n}$  but is more accurately discovered using a numerical optimization scheme that accounts for the laser light's Doppler shift due to the light sail's increasing velocity. The combined effects of changes in  $\overline{\alpha}_{\!\perp}$  and  $\varepsilon_{\rm e}$  can be most clearly seen in the  $T_{\rm max}$  values of Figure 3e. In particular, at low diameters, as  $d_s$  decreases, the ratio  $\frac{\overline{\alpha_{i}}}{\varepsilon}$  increases, leading to higher sail temperatures. In addition, we may observe that  $\overline{Q}$  (Figure 3j) increases with

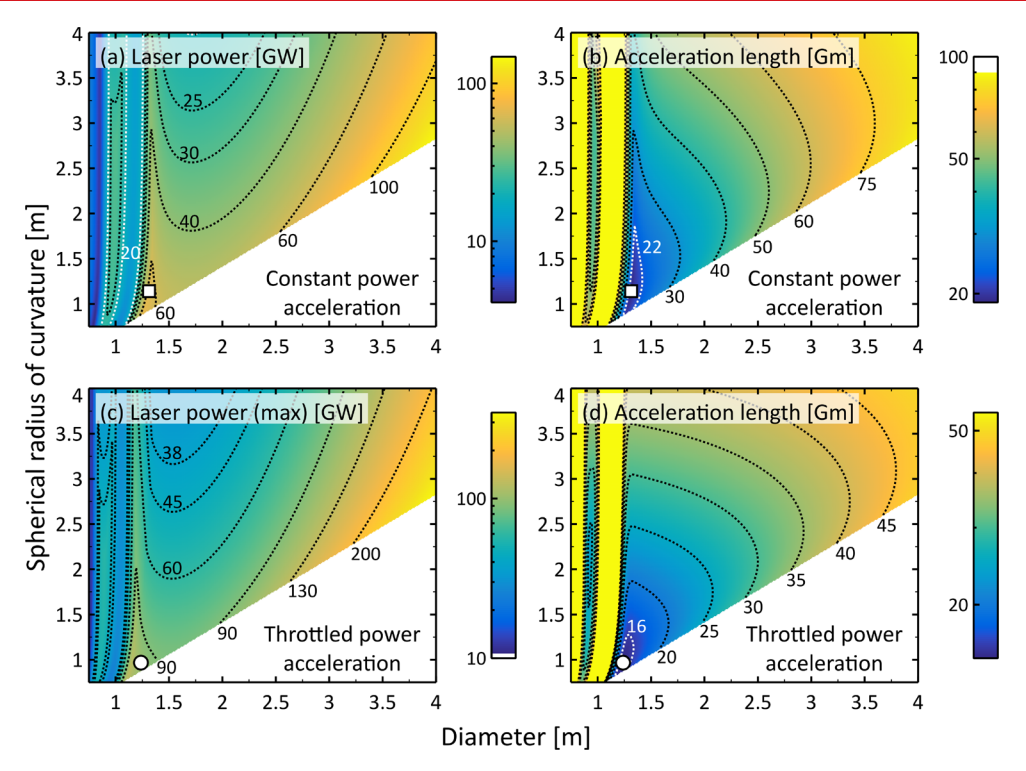


Figure 4. Laser output power  $\Phi_l$  and acceleration length L for a  $m_{\text{tot}} = 2$  g sailcraft composed of the effective  $\text{MoS}_2/\text{Al}_2\text{O}_3$  hybrid material using constant laser output power acceleration (top row) and throttled laser output power acceleration (bottom row), with  $\lambda_l = 1.2 \ \mu\text{m}$ ,  $v_f = \frac{c}{5}$ , and  $\xi = 0.001$ . The squares and circles denote the  $d_s - s_s$  designs exhibiting the minimum values of L for constant laser output power and throttled laser output power acceleration, respectively. The designs shown in this figure have the same  $m_s$ ,  $t_{\bar{p}} \ \overline{Q_a}$ ,  $\overline{\alpha_L}$ , and  $\varepsilon_e$  values as those displayed in Figure 3a,b,j-l, respectively.

increasing  $s_s$ . This arises primarily because flatter sails (larger  $s_s$ ) produce a larger reflected component in the longitudinal direction (back toward the laser) and because off-perpendicular polarization-averaged reflectivity values, occurring at the perimeter of a curved sail, are generally lower than normalincidence values. The effects of this spherical radius of curvature-dependent reflectivity are most evident in the acceleration length L values of Figure 3g, which reveal that, for limited laser output power, somewhat flatter sails achieve lower acceleration lengths (in Figure 3,  $\Phi_1$  = 30 GW is held constant for all  $d_s$ - $s_s$  sail designs). Next-generation light sail designs must account for curvature in reflectivity calculations in order to correctly predict acceleration lengths. Finally, we note that the maximum photon pressure  $P_{\text{max}}$  contour shapes in Figure 3c differ from those of the average reflectivity  $\overline{Q}$ (Figure 3j) because  $P_{\text{max}}$  depends on  $\varrho_{\perp}$  (not shown in Figure 3) rather than on  $\varrho_a$  (see Section S7 in the Supporting Information).

What remains is to demonstrate that, if sufficient laser output power is available, curved light sails will achieve shorter acceleration distances L in comparison to their flatter counterparts. Figure 4 shows this for two alternative laser power modulation approaches. In the top row, for each  $d_s - s_s$  sail design, we determined the constant laser output power  $\Phi_{l,0}$  that would cause a sail to come within a margin of failure  $\xi = 0.001$  of its thermal or mechanical limit at least one instant during its acceleration phase (see Section S11 in the Supporting Information). In the bottom row, again for each  $d_s - s_s$  sail design, we determined the varying laser output power  $\Phi_{l,\beta}$  such that a sail would have a constant margin of failure  $\xi = 0.001$  at all relative velocities  $0 \le \beta = \binom{\nu}{s} \le 0.2$  throughout its

acceleration phase; this is known as laser output power throttling. Figure 4a,c show the  $\Phi_{\rm l,0}$  values and the  $\Phi_{\rm l,max}$  results, respectively, and Figure 4b,d show the calculated L values. The minimum L values are seen to occur in sails with small diameters and significant curvature (small  $s_{\rm s}$ ), reflecting our earlier observation that curvature decreases the stress and strain felt by light sails and allows them to endure greater laser power levels. Finally, we mention that, since beam-riding stability requirements dictate that the center of mass of the sail—tether—chip system must be farther from the sail than the sail's focal point  $f \sim \frac{s_{\rm s}}{2}$ , low  $s_{\rm s}$  values have an additional benefit in that they allow for shorter sail—chip tether lengths and hence lower tether masses. <sup>21</sup>

Looking ahead, while our study assumes a simple baseline design of a spherically curved uniform-thickness single-layer sail, we expect that many of the tradeoffs discussed above will transfer to more complex future designs. We provide three examples, from optical, stability, and mechanical standpoints. First, recent photonic engineering studies of light sails have proposed methods to reduce the film thickness or mass required to achieve adequate optical properties. 13-16,20 However, even such engineered structured films will experience significant photon pressure and could tear if too thin or, if too thick and massive, will accelerate slowly even though highly reflective. Second, stability calculations have suggested that alternative light sail shapes, such as spheres (i.e., ball shapes)<sup>22</sup> or convex curves (i.e., light sails curved away from the laser beam)<sup>27</sup> may offer advantages in terms of beamriding stability. Even these geometries must sustain photon pressures of magnitudes similar to those we show here; curvature can reduce the resulting tensile or compressive

stresses and strains to manageable levels. Third, from a mechanical standpoint, a lightweight substrate or frame could be designed to carry most of the pressure load, relieving some of the stresses on the sail membrane. 9,16 However, just like our simple spherically curved sail, such a support structure would still experience significant stresses and be subject to size, weight, and material tradeoffs. For instance, a backbone composed of tensioned cables would require a material with a mass-specific strength  $\varsigma \equiv \frac{\sigma_{\rm yield}}{\rho}$  that scaled as  $\varsigma_{\rm b} \sim 2 \varsigma_{\rm m} \frac{m_{\rm s,m}}{m_{\rm s,b}}$ where subscripts b and m denote the backbone and the sail membrane, respectively,  $m_{\rm s,h}$  and  $m_{\rm s,m}$  are the masses of the sail backbone and sail membrane, respectively, and  $m_{\rm s,b} \ll m_{\rm s,m}$ (see Section S12 in the Supporting Information). Thus, engineers of next-generation light sails must consider mechanical factors such as those we describe in order to optimize performance and ensure sail viability.

To summarize, we have observed that photon pressures and sail temperatures increase dramatically for realistically short acceleration lengths, such that mechanical factors constrain feasible light sail designs. A convenient method to alleviate excessive stress and strain is to allow light sails to curve, i.e. to bow or billow, as they accelerate, and a general rule of thumb is that a light sail's spherical radius of curvature should be comparable to its diameter. We also observed that the sail's effective reflectivity decreases as it becomes more curved (i.e., as its spherical radius of curvature decreases), suggesting a tradeoff between the sail's mechanical integrity and its optical attributes that should be included in next-generation light sail models. Additionally, we used a new figure of merit to find designs that achieve low acceleration lengths and are also mechanically and thermally robust. Finally, we demonstrated that, given sufficient and variable laser output power, increasing a light sail's curvature allows it to achieve lower acceleration distances. We expect that the main tradeoffs discussed in this paper will still apply to future, more complex designs, ultimately enabling unprecedented investigations of deep space, including the Oort cloud and the Alpha Centauri system.

### ASSOCIATED CONTENT

### Supporting Information

The Supporting Information is available free of charge at https://pubs.acs.org/doi/10.1021/acs.nanolett.1c03272.

Derivations of the equations used in this work and complex refractive index data for  $Al_2O_3$  and  $MoS_2$  (PDF)

## AUTHOR INFORMATION

# **Corresponding Author**

Igor Bargatin — Department of Mechanical Engineering and Applied Mechanics, University of Pennsylvania, Philadelphia, Pennsylvania 19104, United States; ⊚ orcid.org/0000-0003-0305-9932; Email: bargatin@seas.upenn.edu

### **Authors**

Matthew F. Campbell — Department of Mechanical Engineering and Applied Mechanics, University of Pennsylvania, Philadelphia, Pennsylvania 19104, United States

John Brewer – Department of Materials Science and Engineering, University of California at Los Angeles, Los Angeles, California 90024, United States; o orcid.org/0000-0003-1878-8863

Deep Jariwala — Department of Electrical and Systems Engineering, University of Pennsylvania, Philadelphia, Pennsylvania 19104, United States; orcid.org/0000-0002-3570-8768

Aaswath P. Raman – Department of Materials Science and Engineering, University of California at Los Angeles, Los Angeles, California 90024, United States

Complete contact information is available at: https://pubs.acs.org/10.1021/acs.nanolett.1c03272

#### **Notes**

The authors declare no competing financial interest.

### ACKNOWLEDGMENTS

We thank Prof. Prashant K. Purohit for useful discussions about thin film mechanics, as well as Dr. Mohsen Azadi, Thomas J. Celenza, Dr. Pawan Kumar, Jason Lynch, and George A. Popov for insightful comments. This work was supported by the Breakthrough Initiatives, a division of the Breakthrough Prize Foundation. It was also funded in part by a National Science Foundation CAREER award under grant CBET-1845933. J.B. is supported by a National Science Foundation Graduate Research Fellowship under grants DGE-1650605 and DGE-2034835. We thank NASA for the Earth image in Figure 1<sup>39</sup> and the Earth and galaxy images in the table of contents graphic. <sup>57,58</sup>

### REFERENCES

- (1) Cohen, S. A.; Swanson, C.; Mcgreivy, N.; Raja, A.; Evans, E.; Jandovitz, P.; Khodak, M.; Pajerj, G.; Rognuen, T. D.; Thomas, S.; Paluszek, M. Direct fusion drive for interstellar exploration. *J. Br. Interplanet. Soc.* **2019**, 72, 37–50.
- (2) O'Reilly, D.; Herdrich, G.; Kavanagh, D. F. Electric propulsion methods for small satellites: A review. *Aerospace* **2021**, *8*, 22.
- (3) Wagner, K.; et al. Imaging low-mass planets within the habitable zone of  $\alpha$  Centauri. *Nat. Commun.* **2021**, *12*, 922.
- (4) Meech, K. J.; et al. A brief visit from a red and extremely elongated interstellar asteroid. *Nature* **2017**, *552*, 378–381.
- (5) Niccolai, L.; Bassetto, M.; Quarta, A. A.; Mengali, G. A review of Smart Dust architecture, dynamics, and mission applications. *Prog. in Aerosp. Sci.* **2019**, *106*, 1–14.
- (6) Forward, R. L. Roundtrip interstellar travel using laser-pushed lightsails. J. Spacecr. Rockets 1984, 21, 187–195.
- (7) Lubin, P. A roadmap to interstellar flight. J. Br. Interplanet. Soc. **2016**, 69, 40–72.
- (8) Parkin, K. L. G. The Breakthrough Starshot system model. *Acta Astronaut.* **2018**, *152*, 370–384.
- (9) Atwater, H. A.; Davoyan, A. R.; Ilic, O.; Jariwala, D.; Sherrott, M. C.; Went, C. M.; Whitney, W. S.; Wong, J. Materials challenges for the Starshot lightsail. *Nat. Mater.* **2018**, *17*, 861–867.
- (10) Dumusque, X.; Pepe, F.; Lovis, C.; Ségransan, D.; Sahlmann, J.; Benz, W.; Bouchy, F.; Mayor, M.; Queloz, D.; Santos, N.; Udry, S. An Earth-mass planet orbiting  $\alpha$  Centauri B. *Nature* **2012**, 491, 207–211.
- (11) Anglada-Escudé, G.; et al. A terrestrial planet candidate in a temperate orbit around Proxima Centauri. *Nature* **2016**, 536, 437–440.
- (12) Damasso, M.; et al. A low-mass planet candidate orbiting Proxima Centauri at a distance of 1.5 AU. *Sci. Adv.* **2020**, *6*, eaax7467. (13) Ilic, O.; Went, C. M.; Atwater, H. A. Nanophotonic heterostructures for efficient propulsion and radiative cooling of relativistic light sails. *Nano Lett.* **2018**, *18*, 5583–5589.

- (14) Myilswamy, K. V.; Krishnan, A.; Povinelli, M. L. Photonic crystal lightsail with nonlinear reflectivity for increased stability. *Opt. Express* **2020**, *28*, 8223–8232.
- (15) Salary, M. M.; Mosallaei, H. Photonic metasurfaces as relativistic light sails for Doppler-broadened stable beam-riding and radiative cooling. *Laser Photonics Rev.* **2020**, *14*, 1900311.
- (16) Jin, W.; Li, W.; Orenstein, M.; Fan, S. Inverse design of lightweight broadband reflector for relativistic lightsail propulsion. *ACS Photonics* **2020**, *7*, 2350–2355.
- (17) Tung, H.-T.; Davoyan, A. Light-sail photonic design for fast-transit Earth orbital maneuvering and interplanetary flight. 2021, 2107.09121. arXiv. URL: https://arxiv.org/abs/2107.09121 (Accessed July 20, 2021).
- (18) Kudyshev, Z. A.; Kildishev, A. V.; Shalaev, V. M.; Boltasseva, A.; Optimizing, S. Optimizing Startshot lightsail design: A generative network-based approach. 2021, 2108.12999. *arXiv*. URL: https://arxiv.org/abs/2108.12999 (Accessed September 1, 2021).
- (19) Holdman, G. R.; Jaffe, G. R.; Jang, M. S.; Feng, D.; Kats, M. A.; Brar, V. W. Thermal runaway of silicon-based laser sails. 2021, 2110.06185. arXiv. URL: https://arxiv.org/abs/2110.06185 (Accessed October 13, 2021).
- (20) Brewer, J.; Campbell, M. F.; Kumar, P.; Kulkarni, S.; Jariwala, D.; Bargatin, I.; Raman, A. P. Multi-scale photonic emissivity engineering for relativistic lightsail thermal regulation. 2021, 2106.03558. *arXiv.* URL: https://arxiv.org/abs/2106.03558 (Accessed September 15, 2021).
- (21) Popova, E.; Efendiev, M.; Gabitov, I. On the stability of a space vehicle riding on an intense laser beam. *Math. Meth. Appl. Sci.* **2017**, 40, 1346–1354.
- (22) Manchester, Z.; Loeb, A. Stability of a light sail riding on a laser beam. *Astrophys. J. Lett.* **2017**, 837, L20.
- (23) Srivastava, P. R.; Chu, Y.-J. L.; Swartzlander, G. A. Stable diffractive beam rider. *Opt. Lett.* **2019**, *44*, 3082–3085.
- (24) Siegel, J.; Wang, A. Y.; Menabde, S. G.; Kats, M. A.; Jang, M. S.; Brar, V. W. Self-stabilizing laser sails based on optical metasurfaces. *ACS Photonics* **2019**, *6*, 2032–2040.
- (25) Gao, R.; Kim, Y.; Kim, L.; Kelzenberg, M. D.; Ilic, O.; Atwater, H. A. Self-stabilizing silicon nitride lightsails. *Conference on Lasers and Electro-Optics* **2020**, SF3J.6.
- (26) Srivastava, P. R.; Swartzlander, G. A. Optomechanics of a stable diffractive axicon light sail. *Eur. Phys. J. Plus* **2020**, *135*, 570.
- (27) Gieseler, N.; Rahimzadegan, A.; Rockstuhl, C. Self-stabilizing curved metasurfaces as a sail for light-propelled spacecrafts. *Opt. Express* **2021**, *29*, 21562–21575.
- (28) Shirin, A.; Schamiloglu, E.; Sultan, C.; Yang, Y.; Benford, J.; Fierro, R. Modeling and stability of a laser beam-driven sail. 2021 American Control Conference (ACC) 2021, 4269–4275.
- (29) Rafat, M. Z.; Dullin, H. R.; Kuhlmey, B. T.; Tuniz, A.; Luo, H.; Roy, D.; Skinner, S.; Alexander, T. J.; Wheatland, M. S.; de Sterke, C. M. Self-stabilization of light sails by damped internal degrees of freedom. 2021, 2106.10961. *arXiv.* URL: https://arxiv.org/abs/2106. 10961 (Accessed June 22, 2021).
- (30) Early, J. T.; London, R. A. Dust grain damage to interstellar vehicles and lightsails. *J. Br. Interplanet. Soc.* **2015**, *68*, 205–210.
- (31) Hoang, T.; Lazarian, A.; Burkhart, B.; Loeb, A. The interaction of relativistic spacecrafts with the interstellar medium. *Astrophys. J.* **2017**, 837, 5.
- (32) Hoang, T.; Loeb, A. Electromagnetic forces on a relativistic spacecraft in the interstellar medium. *Astrophys. J.* **2017**, *848*, 31.
- (33) Zhang, J.; Wu, N.; Tong, A.; Liu, Y. Structural dynamic responses of a stripped solar sail subjected to solar radiation pressure. *Chin. J. Aeronaut* **2020**, *33*, 2204–2211.
- (34) Huang, X.; Zeng, X.; Circi, C.; Vulpetti, G.; Qiao, D. Analysis of the solar sail deformation based on the point cloud method. *Adv. Space Res.* **2021**, *67*, 2613–2627.
- (35) Savu, D.; Higgins, A. J. Structural stability of a lightsail for laser-driven propulsion. *AIAA Propulsion and Energy 2020 Forum*; 2020. DOI: DOI: 10.2514/6.2020-3842.

- (36) Heinrich, H. G.; Jamison, L. R., Jr. Parachute stress analysis during inflation and at steady state. J. Aircr. 1966, 3, 52-58.
- (37) Gordon, J. E. Structures or Why things don't fall down; Plenum Press: 1978; Chapter 6, Tension structures and pressure vessels with some remarks on boilers, bats, and Chinese junks.
- (38) Timoshenko, S.; Woinowsky-Krieger, S. *Theory of plates and shells*; McGraw-Hill: 1959; Chapter 3, Symmetrical bending of circular plates.
- (39) NASA Image and Video Library. URL: https://images.nasa.gov/details-PIA00342 (Accessed December 6, 2021), Image ID: PIA00342, 1998.
- (40) Lingart, Y. K.; Petrov, V. A.; Tikhonova, N. A. Optical-properties of leucosapphire at high-temperatures. I. Translucent region. *High Temp.* **1982**, *20*, 706–713.
- (41) Querry, M. R. Defense Technical Information Center. URL: https://apps.dtic.mil/sti/citations/ADA158623 (Accessed December 6, 2021), Report ID: ADA158623, Title: Optical Constants, 1985.
- (42) Ermolaev, G. A.; Stebunov, Y. V.; Vyshnevyy, A. A.; Tatarkin, D. E.; Yakubovsky, D. I.; Novikov, S. M.; Baranov, D. G.; Shegai, T.; Nikitin, A. Y.; Arsenin, A. V.; Volkov, V. S. Broadband optical properties of monolayer and bulk MoS<sub>2</sub>. npj 2D Mater. Appl. 2020, 4, 21
- (43) Cannon, P. Melting point and sublimation of molybdenum disulphide. *Nature* **1959**, *183*, 1612–1613.
- (44) Cui, S.; Hu, B.; Ouyang, B.; Zhao, D. Thermodynamic assessment of the Mo-S system and its application in thermal decomposition of MoS<sub>2</sub>. *Thermochim. Acta* **2018**, *660*, 44–55.
- (45) Graczykowski, B.; Sledzinska, M.; Placidi, M.; Saleta Reig, D.; Kasprzak, M.; Alzina, F.; Sotomayor Torres, C. M. Elastic properties of few nanometers thick polycrystalline MoS<sub>2</sub> membranes: A nondestructive study. *Nano Lett.* **2017**, *17*, 7647–7651.
- (46) Sledzinska, M.; Jumbert, G.; Placidi, M.; Arrighi, A.; Xiao, P.; Alzina, F.; Sotomayor Torres, C. M. Fracturing of polycrystalline MoS<sub>2</sub> nanofilms. *ACS Appl. Electron. Mater.* **2020**, *2*, 1169–1175.
- (47) Tripp, M. K.; Stampfer, C.; Miller, D. C.; Helbling, T.; Herrmann, C. F.; Hierold, C.; Gall, K.; George, S. M.; Bright, V. M. The mechanical properties of atomic layer deposited alumina for use in micro- and nano-electromechanical systems. *Sens. Actuators, A* **2006**, *130–131*, 419–429.
- (48) Jen, S.-H.; Bertrand, J. A.; George, S. M. Critical tensile and compressive strains for cracking of Al<sub>2</sub>O<sub>3</sub> films grown by atomic layer deposition. *J. Appl. Phys.* **2011**, *109*, 084305.
- (49) Haastrup, S.; Strange, M.; Pandey, M.; Deilmann, T.; Schmidt, P. S.; Hinsche, N. F.; Gjerding, M. N.; Torelli, D.; Larsen, P. M.; Riis-Jensen, A. C.; Gath, J.; Jacobsen, K. W.; Mortensen, J. J.; Olsen, T.; Thygesen, K. S. The Computational 2D Materials Database: High-throughput modeling and discovery of atomically thin crystals. 2D Mater. 2018, 5, 042002.
- (50) Ilic, O. Nanophotonic materials for space applications. *MRS Bull.* **2020**, 45, 769–778.
- (51) Kulkarni, N.; Lubin, P. M.; Zhang, Q. Relativistic solutions to directed energy. Planetary Defense and Space Environment Applications 2016, 998106.
- (52) Sakamoto, H.; Miyazaki, Y.; Park, K. C. Finite element modeling of sail deformation under solar radiation pressure. *J. Spacecr. Rockets* **2007**, *44*, 514–521.
- (53) Kulkarni, N.; Lubin, P.; Zhang, Q. Relativistic spacecraft propelled by directed energy. *Astron. J.* **2018**, *155*, 155.
- (54) Kipping, D. Relativistic light sails. Astron. J. 2017, 153, 277.
- (55) Kipping, D. Erratum: "Relativistic light sails. Astron. J. 2018, 155, 103.
- (56) Macleod, H. A. Thin-film optical filters, 5th ed.; CRC Press: 2017; Chapter 2: Basic theory.
- (57) NASA Image and Video Library, URL: https://images.nasa.gov/details-PIA18033 (Accessed December 6, 2021), Image ID: PIA18033, 2012.
- (58) NASA Image and Video Library, URL: https://images.nasa.gov/details-GSFC\_20171208\_Archive\_e000268 (Accessed December 6, 2021), Image ID: GSFC\_20171208\_Archive\_e000268, 2017.